A neural network trained by 3D printed biomimetic cochleae provides clinical informatics for cochlear implant patients

Iek Man Lei [1,2], Chen Jiang[3,1], Chon Lok Lei[4], Simone Rosalie de Rijk[3], Yu Chuen Tam[5], Michael P.F. Sutcliffe[1], George G. Malliaras[1], Manohar Bance[3,*], Yan Yan Shery Huang[1,2,*,#]

[1]*Department of Engineering, University of Cambridge, United Kingdom*

[2]*The Nanoscience Centre, University of Cambridge, United Kingdom*

[3]*Department of Clinical Neurosciences, University of Cambridge, United Kingdom*

[4]*Department of Computer Science, University of Oxford, United Kingdom*

[5]*Emmeline Centre for Hearing Implants, Addenbrookes Hospital, Cambridge, United Kingdom*

*Corresponding authors: mlb59@cam.ac.uk, yysh2@cam.ac.uk

[#]Lead contact: yysh2@cam.ac.uk

Abstract

Cochlear implants (CIs) restore hearing in patients with severe to profound deafness by delivering electrical stimuli inside the cochlea. The high electrical conductivity inside the cochlea, however, causes the electrical stimulus to spread, reducing speech comprehension. Understanding the stimulus spread in an individual patient is hampered by the poor accessibility of the inner ear and by the lack of suitable *in vitro* or *in vivo* models. Here, we report on the development of a neural network model that is informed by measurements in 3D printed biomimetic cochleae with realistic conductivity and anatomy. Using four geometric features captured in patients' pre-operative CT scans, the model can reconstruct patients' clinical electric field imaging (EFI) profiles arising from off-stimulation positions with a 90% mean accuracy (n=6). Moreover, the model informs the stereotypical cochlear

geometries prone to stimulus spread and replicates the uncommon clinical occurrence of the 'mid-dip' EFI profiles. This work enables on-demand printing of patient-relevant cochlear models for CI testing, and directly reveals individual patient's *in vivo* cochlear tissue resistivity (0.6 – 15.9kΩcm, *n*=16) by CI telemetry.

Introduction

The use of prosthetic medical electronic implants and bioelectronic devices has been increasing rapidly, and is anticipated to form a new era of medicine[1,2]. By delivering local electrical stimuli to tissues, these electronic implants restore lost electrical functions in tissues or nerves, or modulate signalling patterns for therapeutic outcomes[2,3]. Cochlear implants (CIs) are by far the most widely used neuromodulation electronic implants, with well over 500,000 CIs having been implanted worldwide[4], and their prevalence is only expected to grow more rapidly with the projected increase in the elderly population[1]. Bypassing the malfunctioning peripheral auditory mechanisms, the CI electrode array is designed to restore sound perception, and preserves the tonotopic response of the cochlea by delivering programmed stimulation at localised regions of the cochlear lumen; this in turn stimulates separate auditory neural elements[5,6] (Fig.1a), with lower sound frequencies represented apically and higher frequencies basally.

Fig.1: Embedded 3D printing of biomimetic cochleae for reproducing the CI stimulus spread characteristics.

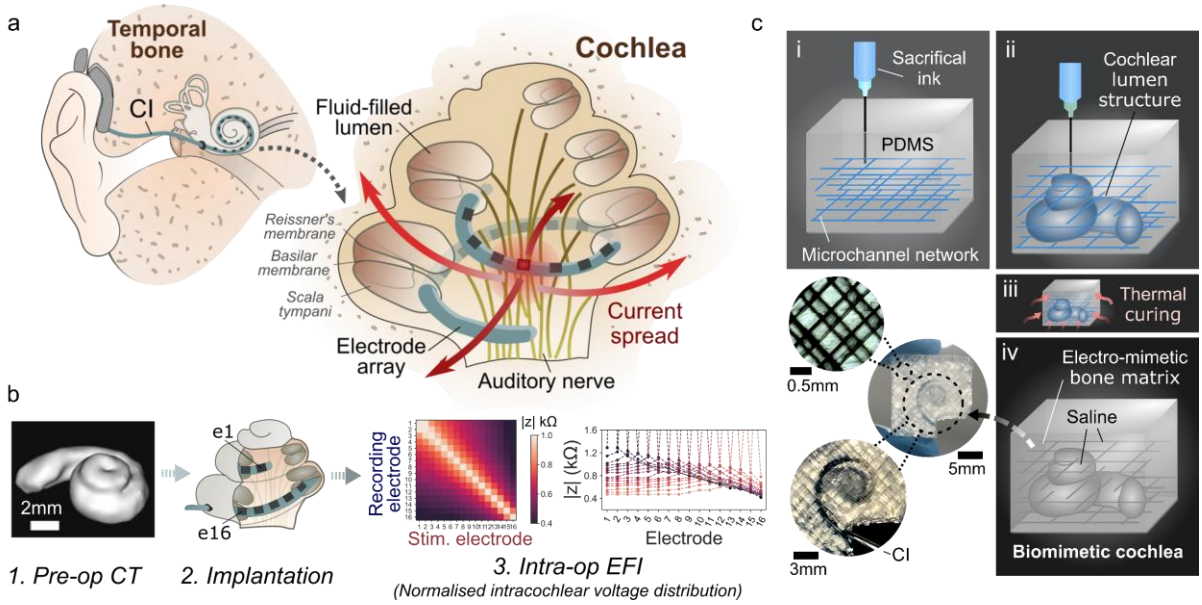

a, Schematic of the auditory system and the cochlea with a CI implanted. The 'current spread' problem induced by a stimulated electrode of the CI electrode array is indicated. **b,** Schematic of the routine CI assessment process; **1.** Routine pre-operative CT scan of a patient's cochlea, which typically only has a resolution to reveal the ensemble spiral-shaped cavity of a cochlea; **2.** Implantation of the electrode array of a CI in the scala tympani of the cochlea; **3.** Acquisition of an EFI (electric field imaging) profile, which is derived from recording the induced intracochlear voltage V measured at each electrode upon injecting consecutive current pulses at each electrode in the array. The voltage measurements are then converted to transimpedance magnitude $|z|$ by normalising the voltage V with the stimulation current impulse I_{stim} ($|z| = V / I_{stim}$). The off-stimulation (off-diagonal) measurements in the EFI present information about the tissue impedance[9]. **c,** Schematic of the embedded 3D printing strategy to produce the electro-mimetic bone matrices and the biomimetic cochleae.

A major limitation of today's electronic implants is their imprecise control of the administered stimulus, arising from the intrinsic conductive nature of biological tissues, and particularly of the biological fluids in the inner ear[4,5,7–9]. This limitation is well exemplified by the 'current spread' problem of CIs, where the uncontrolled spread of electrical stimulus leads to off-target excitation of the neighbouring auditory nerves (thus causing a mismatch or 'smeared' representation in the perceived sound from that intended)[4,9] (Fig.1a). Cochlear

anatomy, tissue conductivity, and implant positioning are suggested to be the primary patient-specific factors controlling the intracochlear voltage distribution induced by CIs[9–12]. In particular, cochlear anatomy (in terms of size and shape) is variable, with different levels of volumetric conductance of cochlear fluids affecting the intracochlear voltage that results from stimulation. Moreover, pathophysiological conditions could affect electrical conductivity of the cochlear bony walls, and thus CI induced electric fields[13]. As the cochlea is embedded deep inside the temporal bone and has a complex anatomy, electrical characteristics are difficult to quantify in a living subject. As a result, a model that deciphers how the biologic characteristics of a patient's cochlea affect the stimulus spread would be a valuable tool for predicting and optimizing the stimulus signals that ultimately result in better sound perception and speech recognition. It may also provide insights into factors controlling the large variation in patient-specific CI performance.

Although various physical and computational models have been developed for CI testing[9,12,14–16], they are incomplete in evaluating the stimulus spread in human cochleae. Animal models are well-established for *in vivo* CI testing, but due to the drastic differences between the cochlear anatomies of humans and animals[17], very incomplete insights into human responses are obtained[1,3]. Though human cadavers can provide anatomical fidelity, they are limited in supply and have altered electrical properties due to preservation and post-mortem changes[18]. *In silico* approaches, such as finite element modelling (FEM), can overcome ethical, sample availability and cost issues[19]. However, existing FEM modelling is limited by several factors, including scant knowledge of the electrical properties of live human cochleae tissues to fit different *in vivo* cases[20], the inability to capture patient-dependent anatomical-guided CI positioning, and the under-determined boundary conditions[14].

To establish a robust modelling framework for interpreting clinical CI testing data, we created a library of 3D printed cochlear models (*n*=82) which captures the diverse geometry of the human cochlear lumen along with a spectrum of bone tissue resistivities within the reported range obtained from *in vivo* human studies. Supplementary Video 1 shows CT scans of exemplar 3D printed biomimetic cochleae. Using these models, a broad spectrum of clinically representative electric field imaging (EFI) profiles (normalised intracochlear voltage distribution along the CI electrode array) was acquired by varying the model electro-anatomical characteristics. Then, by inputting EFI profiles from the biomimetic cochleae as the training dataset, we establish a neural network model termed 3PNN (3D printing and neural network co-modelling), which provides powerful clinical informatics such as deciphering patient-specific attributes of CI current spreads, and extracting patient-dependent cochlear tissue resistivity.

Results

Designable electro-mimetic bone matrices

The human cochlea is a spiral-shaped hollow organ embedded in the temporal bone (Fig.1a). Since there were no established reports of *in vivo* cochlear tissue conductivities, our first goal was to establish a printable material system that could emulate the range of reported bone tissue conductivities (thereafter, termed electro-mimetic bone matrix). *In vivo* human studies during surgery estimated that the electrical resistivities of human skulls vary widely between 0.6 to 26.6 kΩcm, depending on the site, composition, age and porosity[21–25] (Supplementary Fig.1a-b).

To reproduce the mesoscale electrical properties of bone, we take inspiration from the micro-architecture of bones, which consists of conductive fluid-filled interconnected pores surrounded by a poorly conductive mineralised phase[26]. Thus, we structured an electro-mimetic bone matrix that exhibits interconnected saline-filled channels inside a crosslinked PDMS (polydimethylsiloxane) elastomer. The interconnected channels were created by embedded printing a Pluronic F127 sacrificial ink in pre-crosslinked PDMS (Fig.1c, Supplementary Video 2), permitting flexible and precise tuning of the void density and, therefore, the resistivity of the electro-mimetic bone matrices (Supplementary Fig.2). Comparing our printing method with stereolithography, Pluronic F127 can be easily removed after printing[27] and further enhances the wettability of PDMS due to its amphiphilic nature. The channels were then filled with a physiological saline, which we hypothesise is important to emulate the electrical impedance properties of bone tissues, as pores in bone would normally be wet with extracellular fluids. The electrochemical impedance spectroscopy (EIS) measurements in Fig.2a and Supplementary Fig.3 show that an electro-mimetic bone matrix can be designed to exhibit impedance properties matching those of a human cadaveric cochlear bone, for the operating frequencies of CIs (i.e. f=1-100 kHz). By varying the void fraction in the electro-mimetic bone matrix from 20% to 84%, the resistivity of the matrix can be tuned from 0.2 to 22 kΩcm (Fig.2b), covering almost the entire reported resistivity range of live human skull tissues[21–25] (0.6 – 26.6 kΩcm, Fig.2c).

Fig.2: Electrical properties of electro-mimetic bone matrices.

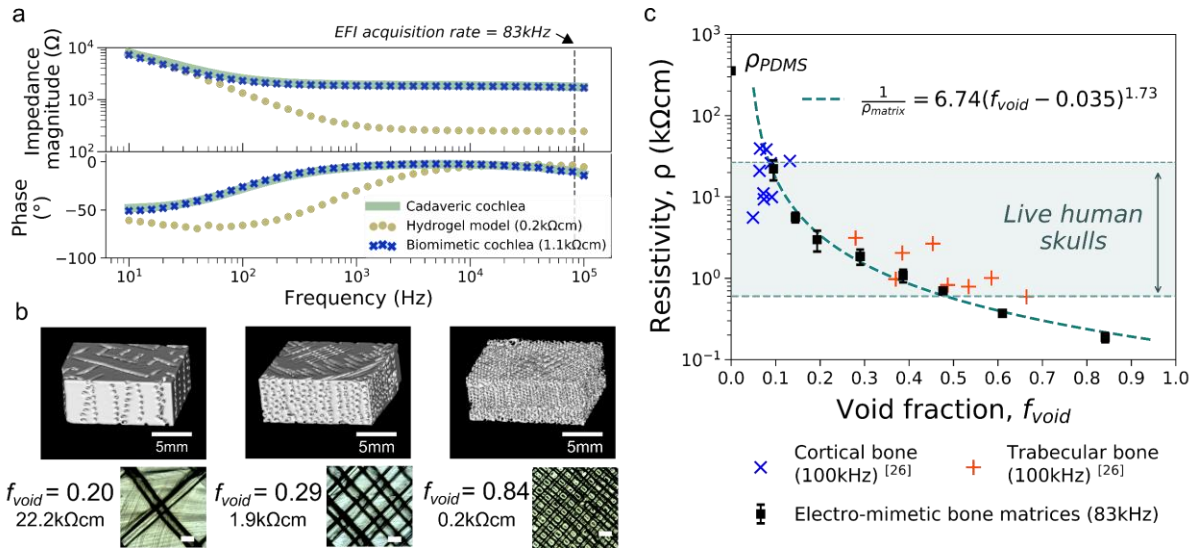

a, Bode plot showing the impedance properties of a cadaveric cochlea, and 3D printed cochlear models made of an electro-mimetic bone matrix and a hydrogel. **b,** Micro-CT reconstructed images (top) and optical microscopic images (bottom) of the electro-mimetic bone matrices at different volumetric void fractions (f_{void}). Scale bar of the optical microscopic images = 500µm. The resistivities of the matrices were measured at 83kHz, the EFI acquisition rate used in this study[28]. **c,** Resistivity of the electro-mimetic bone matrices ($n \geq 3$) as a function of f_{void}, compared to the reported resistivities of bovine cortical and trabecular bones[26]. The relationship between the resistivity of the electro-mimetic bone matrix and f_{void} is well-described by a percolation equation of a conductor-insulator composite[29] (Supplementary Fig.2e).

Fig.3 shows a material property chart summarising the electrical resistivity and the Young's modulus for a range of biological tissues and polymeric materials. The 3D printed electro-mimetic bone matrices cover a wide resistivity range, which cannot be imitated by a single printable material (i.e. thermoplastics or hydrogels) alone or a hydrogel-fillers matrix (i.e. bioceramics and PDMS microbeads dispersed in hydrogels) (Supplementary Fig.4a). Apart from electrical resistivity, we suggest that Young's modulus of the model is also an important consideration for electronic implant testing, because the mechanical properties of the implanted tissues will also determine the final position of the CI electrode array inside the cochlea. Adopting PDMS as the solid phase of the electro-mimetic bone matrix not only

facilitates the ease of embedded printing, but also imparts favourable mechanical properties as a CI testing platform. With a Young's modulus in the 10^6 Pa range, we estimate that the force associated with CI electrode insertion will not induce a significant deformation to the matrix (Supplementary Note 1). At the same time, the compliance of the matrix mitigates mechanical damages to the fine electrodes of a CI, which is commonly experienced when inserting CI electrode arrays repeatedly in cadaveric samples (modulus of hard tissues > 10^9 Pa). Hence, multiple insertions can take place for the same CI electrode array, which is of practical importance due to the time-consuming fabrication and costs associated with a CI. Overall, the above results suggest the electro-mimetic bone matrices to be a suitable material system for creating electroanatomical models of human cochleae.

Fig.3: Wide resistivity tuneability and adequate mechanical properties of electro-mimetic bone matrices.

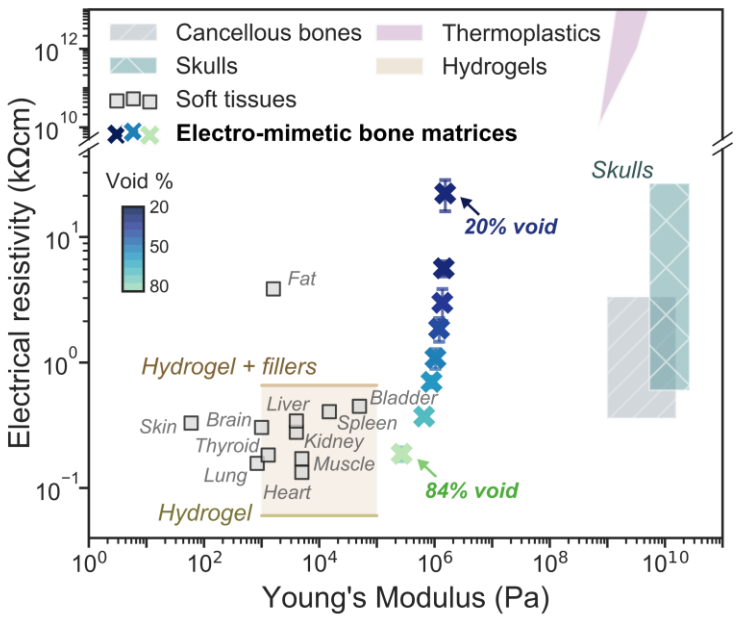

A map of resistivity versus Young's modulus of human tissues, thermoplastics, the hydrogel-fillers matrices, and the electro-mimetic bone matrices tested in this study ($n \geq 3$). The compositions of the hydrogel and hydrogel-fillers matrices tested here are listed in Supplementary Fig.4a. Young's modulus of the electro-mimetic bone matrix was estimated by scaling the Young's modulus of pure PDMS (1.7 MPa at a curing temperature of 60°C[30]) linearly with the f_{void} of the matrix. Tissues and thermoplastics data, and the Young's modulus of hydrogels were compiled from literature[21,22,35,23–26,31–34].

3D printed biomimetic cochleae

Clinically, a CI electrode array is inserted into the scala tympani, one of the three cochlear ducts[13] (Fig.1a). As a coarse-grained approach to replicate the electroanatomical features of a CI implanted cochlea, we approximate the cochlea as one ensemble spiral cavity with continuously narrowing diameter, and omit the inner soft-tissue membranous structures of a cochlea, such as the basilar membrane and Reissner's membrane. This is because, firstly, in a typical patient's pre-operative CT scan as routine clinical assessment (Fig.1b), the scan resolution only permits the identification of the shape of the ensemble cochlear lumen and not the fine microanatomical structures (Supplementary Fig.5); and secondly, our preliminary finite element modelling shows that the effect of the basilar membrane and the Reissner's membrane inside a cochlea on the EFI profile at off-stimulation positions is likely to be insignificant, as the boundary impedances are dominated by surrounding bone tissues (see Supplementary Fig.6 & 7). Therefore, we constructed the biomimetic cochleae by embedded 3D printing a tapered and spiral-shaped cochlear lumen cavity inside an electro-mimetic bone matrix (Fig.1c and Supplementary Video 2). The spiral-shaped cavity was filled with a physiological saline to mimic the ionic conduction milieu in the cochlea (perilymph) (Supplementary Fig.2c) and the conduction properties at the electrode-electrolyte interface.

Fig.4a-b show high-resolution micro-CT scans of a cadaveric cochlea and an exemplar 3D printed biomimetic cochlea with a CI inserted. It is worth noting that the CI electrode-to-spiral centre distance displayed in the 3D printed cochlea matches closely with the electrode-to-modiolus distances measured clinically from patients' CT scans[36] (Supplementary Fig.8). This gives confirmation that the PDMS-based electro-mimetic bone matrix has adequate structural rigidity to provide geometrically-guided implant insertion and positioning. Since the size and the shape of a cochlea is unique to an individual and can vary greatly from

person-to-person, we assign four geometrical descriptors to numerically describe the reported anatomical variations in CI implanted human cochleae[37–39]: they are basal lumen diameter, taper ratio, cochlear width and cochlear height (see definitions in Fig.4c and Supplementary Table 1). For electroanatomical modelling of cochleae, we incorporated a fifth descriptor, the matrix resistivity, which is controlled by the void fraction of the electro-mimetic bone matrix. In total, 82 biomimetic cochleae were printed at different combinations of model descriptors. With this physical model library, we artificially reconstructed a broad spectrum of the electroanatomical features of human cochleae with even feature distributions.

Next, we acquired intracochlear EFI profiles (normalised intracochlear voltage distribution) in our cochlear models with a CI[1J] (Advanced Bionics HiRes 90K® implant with HiFocus™ 1J electrode) inserted. EFI samples the intracochear voltage (V) along the electrode array in response to a current injection or a stimulation impulse (I_{stim}) at each electrode (Fig.1b). The off-stimulation measurements in EFI profiles contain information about the induced voltage spread characteristics of the cochlea. EFIs and similar measures (e.g. transimpedance matrix from Cochlear Corporation® or Impedance Field Telemetry from MED-EL®) are commonly used as part of the routine CI clinical assessment.

Fig.4: 3D printed biomimetic cochleae to replicate the broad anatomical spectrum of human cochleae and give patient-relevant EFI profile.

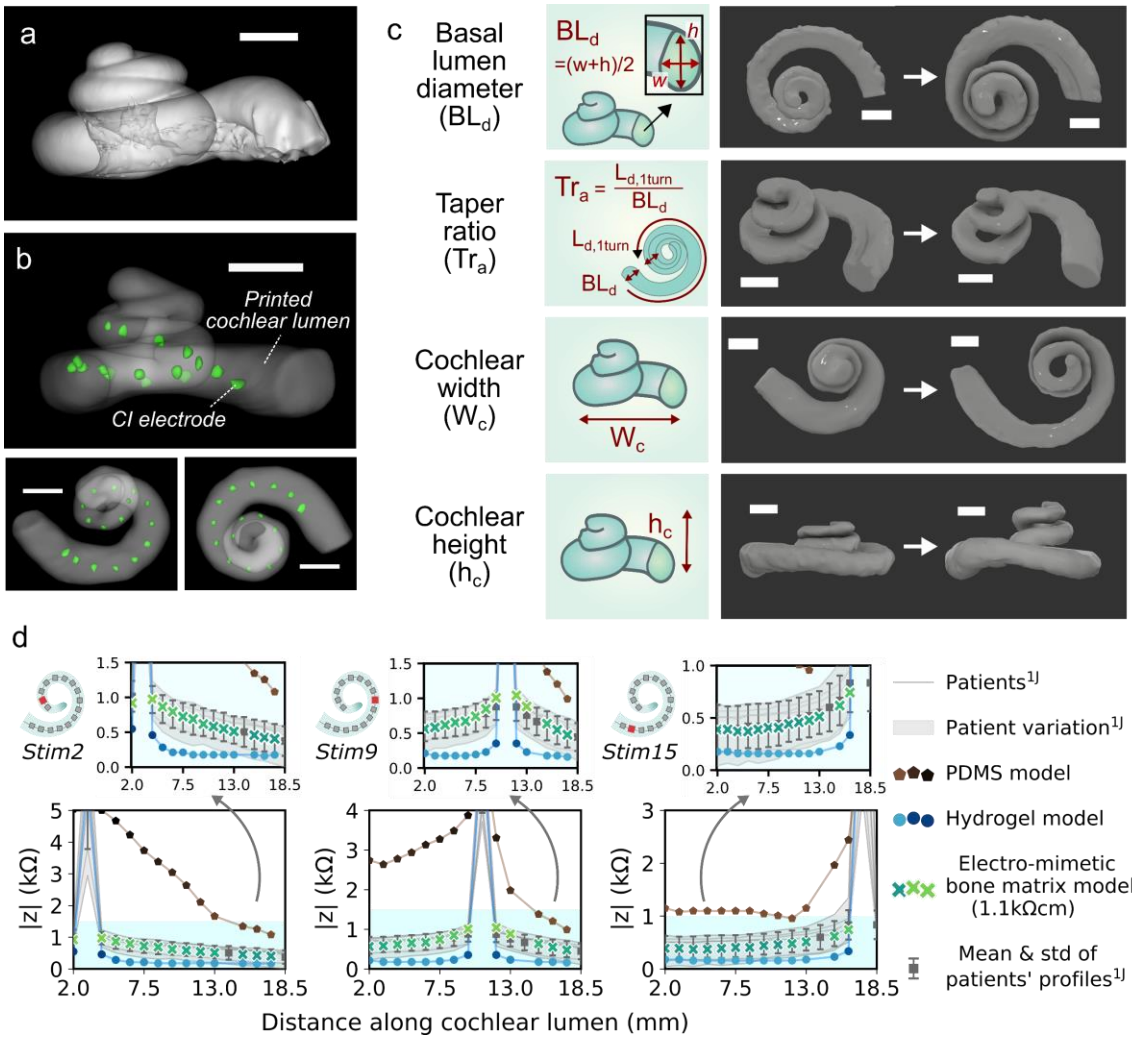

Micro-CT reconstructed images of **(a)** a cadaveric cochlea and **(b)** the lumen of a 3D printed biomimetic cochlea with CI electrode (marked green) implanted. Scale bar = 2mm. **c,** Micro-CT reconstructed images of the spiral cavity of the biomimetic cochlea with different geometric features. Scale bar = 2mm. Four geometric descriptors are used – basal lumen diameter, taper ratio, cochlear width, and cochlear height. Detailed definitions and the range of the descriptors tested in this study can be found in Supplementary Table 1. **d,** Comparison of the mean EFI profile of patients implanted with CI[1J] and the EFI profiles obtained from 3D printed models made of hydrogel, PDMS and electro-mimetic bone matrix. EFI induced by the stimulations of the apical electrode (electrode 2), the medial electrode (electrode 9) and the basal electrode (electrode15) were shown.

To further demonstrate the importance of having a realistic bone matrix resistivity in reproducing the patient EFI profile, we also fabricated models made of materials with

contrasting conduction properties, hydrogels (representing the highly conductive case) and solid PDMS (representing the insulating case). Fig.4d shows the mean patient's EFI profile derived from 6 patients implanted with an Advanced Bionics CI[1J] compared with the EFI profiles of the 3D printed models. We found that the PDMS model led to a steeper and extremely asymmetrical EFI profile (as seen in the stimulation at the medial electrode), strongly mismatched with patient profiles. In comparison, the conductive hydrogel model resulted in a low magnitude EFI profile. By replicating realistic bone resistivities with electro-mimetic bone matrices, our biomimetic cochlea can be designed to match the patient's stimulus spread characteristics.

Clinically validated 3PNN shows high predictive performance

By training a neural network (NN) model with the EFI profiles acquired from the 3D printed biomimetic cochleae, a 3D printing and neural network co-modelling (3PNN) framework (Fig.5a) was established to model the relationship between EFIs and the electroanatomical features of the CI implanted biomimetic cochleae. Reasons for using NN modelling instead of other existing computational models are discussed in Supplementary Note 2 and Supplementary Fig.10. To support various application needs, we developed forward-3PNN and inverse-3PNN. Forward-3PNN is used to predict EFIs arising from different electroanatomical descriptors of a cochlea, coupled with different CI stimulus and recording positions (covering 18.5mm section of a CI from different manufacturers that may have different electrode locations and spacings). Inverse-3PNN has the ability to infer the distribution of the electroanatomical descriptors of a cochlea for a given EFI profile.

We validated the clinical applicability of 3PNN using routinely acquired clinical data. In total, six paired sets of patient's CT scan and EFI profile acquired with a lateral wall CI

(HiRes™ Ultra HiFocus™ SlimJ electrode array, CI^{SlimJ}) were used for validation, an electrode similar to the model test electrode , CI^{1J}. Starting with our forward-3PNN, we predicted patients' EFI profiles at off-stimulation positions based on the four geometric descriptors measured from their CT scans, while assuming the matrix resistivity inputs are equal to a default value of 9.3kΩcm (which is the mean reported resistivity of live human skulls obtained during surgery[21–25], see Supplementary Fig.1a). The predicted off-stimulation EFI profiles (EFI arising from off stimulation positions) match the patients' clinical profiles with a 10% MAPE (mean absolute percentage error) (Fig.5b), considering the limited resolution of patients' cochlear CT scans, and the non-patient specific cochlear resistivity.

We further validated our 3PNN by inversely inferring the distribution of the model descriptors that could match a patient's off-stimulation EFI profile with an average similarity over 92%. Comparing the predicted distributions of the four geometric descriptors with the corresponding patient's features measured from their CT scans, MAPE is less than 10% (Fig.5c). Nevertheless, the predictive quality in cochlear height is less satisfactory compared to the predictions of basal lumen diameter, taper ratio, and cochlear width, which closely match the measured patients' features with MAPE less than 6%.

Fig.5: Clinical Validation of 3PNN.

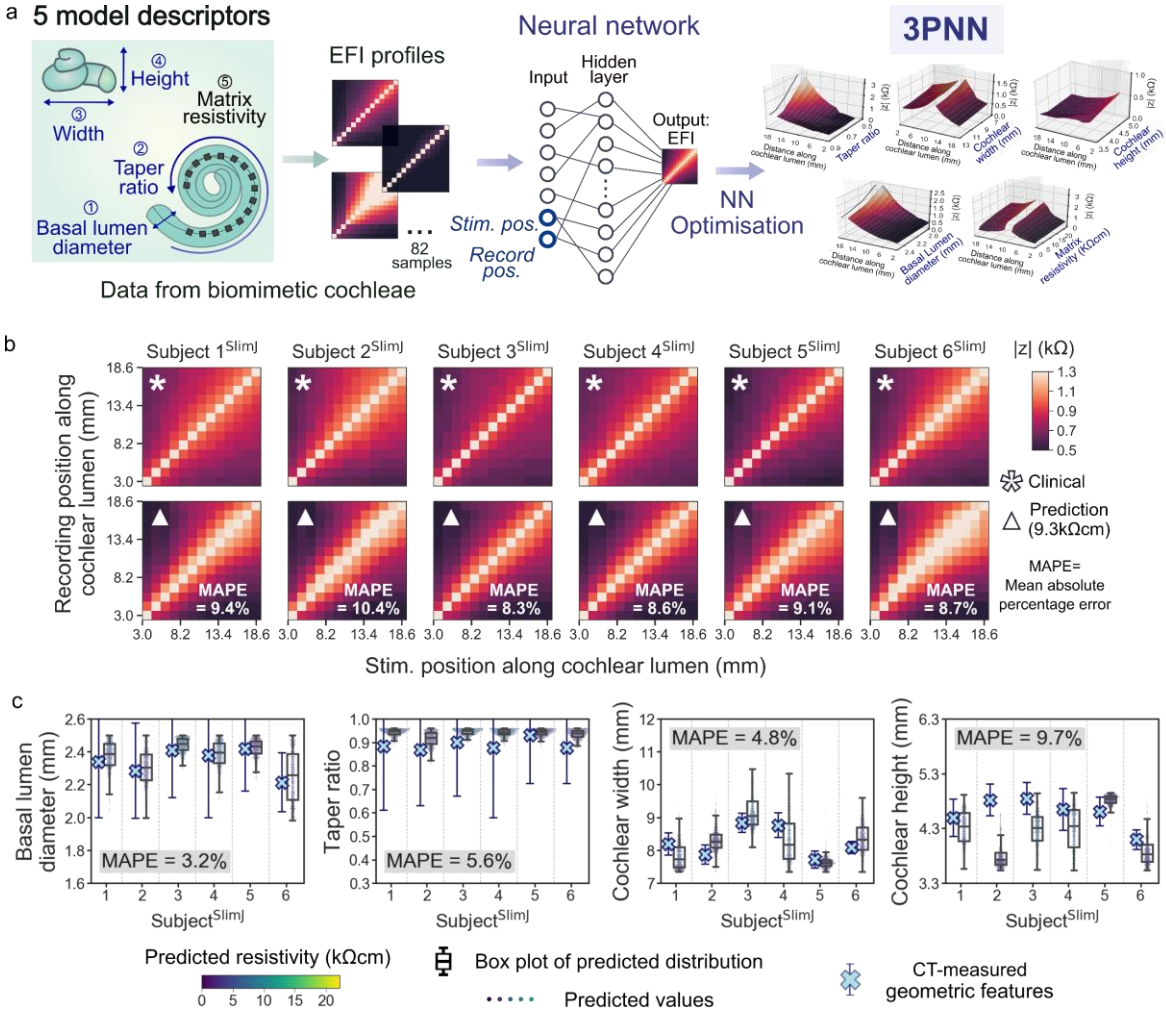

a, Schematic of the workflow of 3PNN. 3PNN was developed by training a neural network model with the EFI profiles acquired from the 3D printed biomimetic cochleae. 3PNN models the mapping from the 5 model descriptors, the stimulus position and the recording position to the EFI profile. The hyperparameters of 3PNN were tuned using 10-fold cross-validation to achieve the best predictive performance (Supplementary Fig.11). **b,** Validation of the forward-3PNN by comparing the patients' clinical EFI profiles with the predicted EFI profiles derived from the geometric descriptors of patients' cochlear CTs at off-stimulation positions. The matrix resistivity inputs were defaulted as the mean reported resistivity of live human skulls (9.3kΩcm). MAPE (mean absolute percentage error) is used to quantify the predictive performance. **c,** Validation of the inverse-3PNN by comparing the patient's geometric descriptors measured from their cochlear CT scans with the predicted distribution of the geometric descriptors that could result in an off-stimulation EFI profile with an average similarity over 92% to the patient's profile. To approximate the predicted distribution of the descriptors, 1000 predicted sets of the model descriptors were plotted for each predicted distribution, and the distribution is depicted by a box plot. Colour of each point denotes the predicted resistivity. Error bars of the patients' CT-measured geometric features were approximated as 1 pixel size of the CT scans.

Effect of cochlear electroanatomy on CI voltage spread

With the validated 3PNN model, we proceeded to investigate how the CI voltage spread characteristics could be affected by the four geometric descriptors and the matrix resistivity. Using forward-3PNN, we simulated EFI profiles by sweeping through different combinations of the 5 model descriptors (examples shown in Supplementary Fig.12). To parameterise the voltage spread characteristics shown in the EFI profiles, we fitted a power law, Equation (1), to each stimulus spread toward the apex and toward the base (detailed examples shown in Supplementary Fig.13).

$$|z| = \frac{V}{I_{stim}} = Ax^{-b} \qquad (1)$$

where $|z|$ = transimpedance magnitude, V = voltage between the recording electrode and the ground electrode, I_{stim}= stimulation impulse current, x = distance along the cochlear lumen from the stimulating electrode, A = baseline coefficient and b = coefficient indicating how fast voltage drops over a distance. The larger the b value, the sharper the voltage drop. The power law relation was adopted here because, theoretically, volume conduction from a point source in a homogeneous medium should follow an inverse relationship with the form of $|z| = \frac{1}{4\pi\sigma r}$, where σ = conductivity of the homogeneous medium and r = distance from the stimulating electrode[40]. The mean fitting coefficients ($\bar{A}_{apex}$, and $\bar{A}_{base}$) were used here to quantify the mean baseline coefficient; and $\bar{b}_{apex}$ and $\bar{b}_{base}$ were used as indicators of the sharpness of voltage drop toward the apex and the base of the cochlea.

As evidenced in Supplementary Fig.14, we confirm that the trend of the magnitude of EFI across each descriptor is independent of other model descriptors. Therefore, we examined the dependence of the mean coefficients $\bar{A}$ and $\bar{b}$ across each model descriptor individually

(Fig.6a). We found that both the geometric descriptors and the matrix resistivity affect the mean baseline coefficient $\bar{A}$, whilst the matrix resistivity in the range we investigated does not seem to play a key role in the voltage drop coefficient, $\bar{b}$. In addition, our findings suggest that the voltage drop is shallower (smaller $\bar{b}$ value) in the following scenarios: cochleae with larger basal lumen diameter, less tapered cochlear lumen (i.e. taper ratio closer to 1) and smaller cochlear width. Therefore, we expect that cochleae with these geometric features have more intracochlear voltage spread, which may activate a larger number of neurones over a broader region. However, the activation function for neurones should also be considered for a more sophisticated prediction of the activation of neurons[41].

On-demand creation of biomimetic cochleae inheriting patient EFIs

The clinical validation of 3PNN demonstrates that the 3D printed cochleae can reproduce the off-stimulation EFIs of CI users with high fidelity, despite the physical simplicity of the models. With such a validated platform, we further demonstrate its application to construct on-demand biomimetic cochleae that can yield patient-specific off-stimulation EFI profiles. To do this, we first used the inverse-3PNN to obtain the distribution of the model descriptors that could match each patient's off-stimulation EFI profile with an average similarity over 90% (Fig.6b and Supplementary Fig.15). Subsequently, embedded 3D printing was used to fabricate a patient-specific biomimetic cochlea exhibiting the features of a set of model descriptors inferred from inverse-3PNN. As shown in Fig.6c, the EFI profiles measured from the 3D printed biomimetic cochleae show good resemblance to their corresponding patients' off-stimulation EFI profiles, with MAPE less than 10%; while the patients' EFI profiles show a dissimilarity of over 30% MAPE.

Fig.6: Broad applicability of 3PNN for clinical informatics.

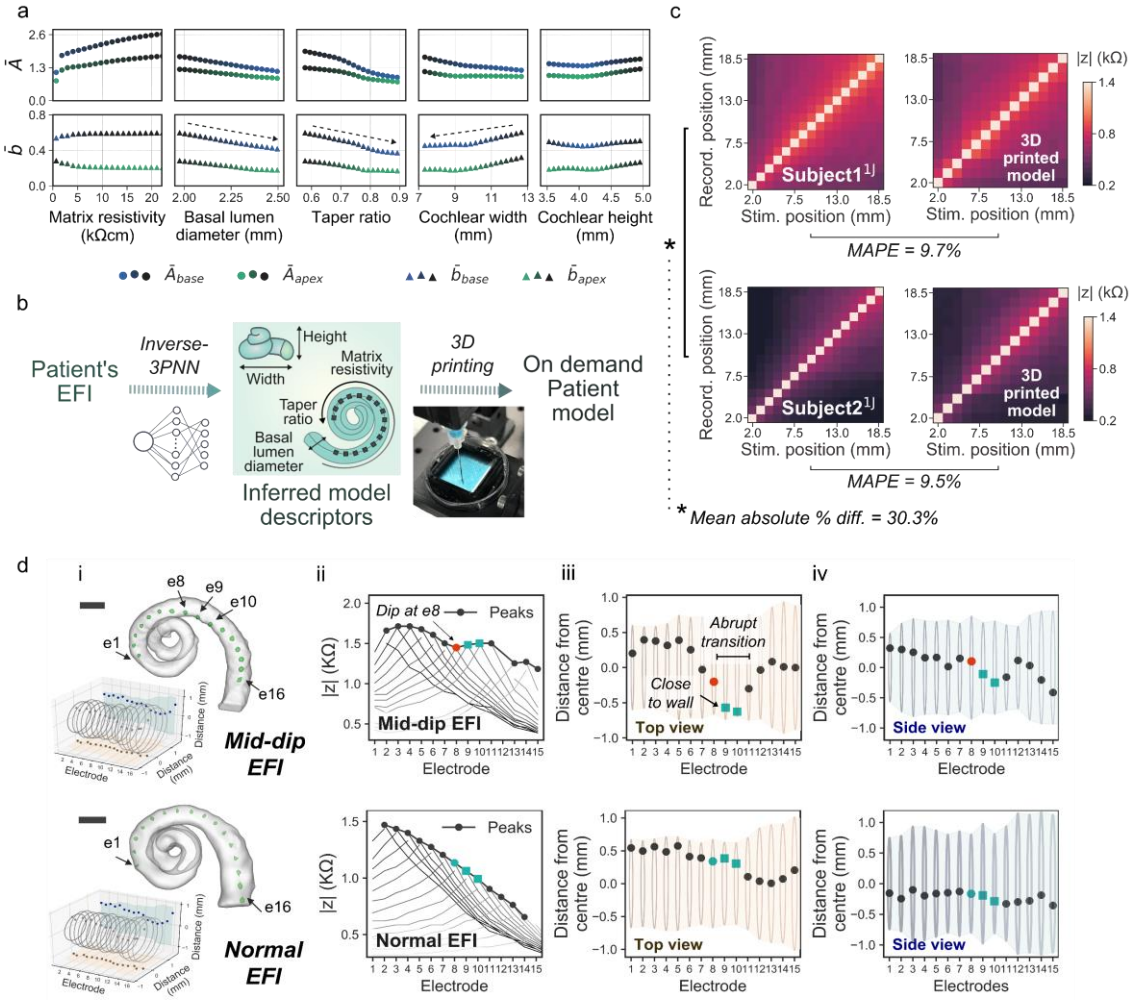

a, The trend of the mean baseline coefficient ($\bar{A}_{apex}$, $\bar{A}_{base}$), and the indicators of the sharpness of voltage drop ($\bar{b}_{apex}$, $\bar{b}_{base}$) toward the apex and toward the base of the cochlea across each model descriptor. The arrow direction indicates the decreasing sharpness of voltage drop in these cochlear features, which suggests an increased voltage spread susceptibility. **b,** Schematic showing the process to generate the patient-specific biomimetic cochlea, where inverse-3PNN was used to deduce the model descriptors best-fitting the patient off-stimulation EFI, and the patient cochlear model was then fabricated by 3D printing with one of the predicted sets of the model descriptors (Supplementary Fig.15). **c,** Comparison of the off-stimulation EFIs of two patients and the off-stimulation EFIs acquired in their corresponding biomimetic cochleae. The model descriptors used to produce the biomimetic cochleae of subject1^{1J} and subject2^{1J} are as follows: matrix resistivity 2.9 versus 0.7kΩcm, and taper ratio 0.9 versus 0.7, respectively, while with similar basal lumen diameter~2.4mm, cochlear width~10.5mm, and cochlear height~4.4mm. **d,** The electrode positions in a model showing an uncommon 'mid-dip' EFI profile (top) and a model with a typical EFI profile (bottom). **(i)** Reconstructed 3D micro-CT volumes of the cochlear lumens of the biomimetic cochleae with a CI electrode array inserted (marked green); **(ii)** EFI profiles of the models; **(iii)** Top view and **(iv)** side view of the cochlear lumens of the models, showing the positions of the electrodes in the models relative to the lumen wall.

Beyond the application of reproducing patient-specific EFI profile with a physical 3D printed model, our platform further points to the potential occurrence of uncommon EFI profiles, such as the 'mid-dip' characteristics occasionally observed in patients. The 'mid-dip' characteristic (Fig.6d), which is distinguished by a dip in the EFI profile at the medial electrodes, has not been given a clear clinical explanation. It is uncertain whether implantation abnormality or patient-specific cochlear biologic properties could be the origin. By visualising the positions of electrodes in our 3D printed models with micro-CT imaging, we found that the electrode position, which was guided by the cochlear geometry, could be a potential explanation. As shown in Fig.6d, the mid-dip characteristics can be produced by a specific combination of cochlear shape and CI positioning. In the model with the 'mid-dip' characteristics, the electrode positions appear to change abruptly (panel iii in Fig.6d), where electrode 8 (e8) was adjacent to two 'near-wall' electrodes (e9 and e10) that were in close proximity to the spiral centre (Supplementary Fig.8). This sudden decrease in the electrode-to-wall distance can potentially cause a slight increase in the EFI profile, hence a dip at e8 in the profile. On the contrary, in the model without the 'mid-dip' characteristics, the electrode positions changed gradually. This suggests that the relative position of the electrode to the neighbouring electrodes and the lumen wall can be one of the factors of the mid-dip abnormality in the EFI profile.

Informing patient-specific cochlear tissue resistivity

As the absolute resistivity of patients' temporal bones near the cochlear vicinity cannot be measured non-invasively in living subjects, our inverse-3PNN further presents a unique capability of deducing the resistivities of patients' cochlear tissues based on their individual EFI profiles. 16 patients implanted with CI^{SlimJ} or CI^{1J} were examined here. Fig.7 shows the ranges of the patient-specific resistivities, which were deduced with paired pre-op CT (thus

known patient geometric descriptors) for subjects^{SlimJ} 1-6 and with unknown geometric descriptors for the rest. The predictions were undertaken with the criterion that the off-stimulation EFI profiles simulated from the inferred sets of the model descriptors are less than 10% MAPE to the patient's profile.

Fig.7: 3PNN informing patient-specific resistivity of the cochlear tissue.

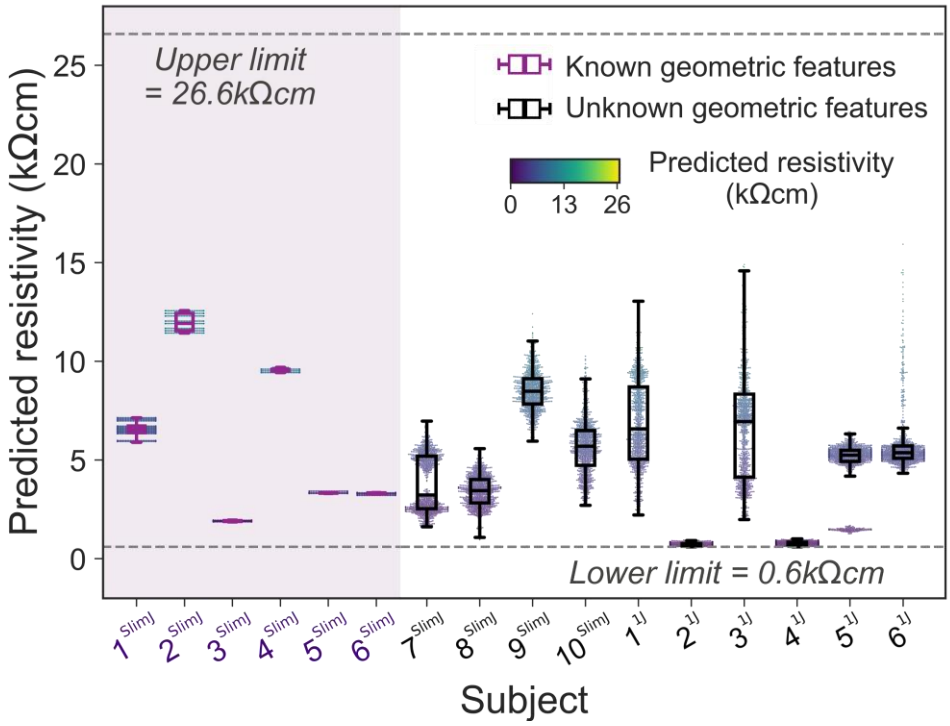

Predictions of subjects 1-6^{SlimJ} were carried out with known patient's geometric descriptors measured from their cochlear CT scans, whereas predictions of subjects 7-10^{SlimJ} and subjects 1-6^{1J} were undertaken where patient's geometric descriptors were unavailable due to restricted access to the patient CT scans. Dotted lines show the reported upper and lower limits of *in vivo* human skull resistivities[21–25].

All the predicted patient resistivity ranges (0.6 – 15.9 kΩcm) lie within the reported resistivity range (0.6 – 26.6 kΩcm) of live human skulls measured during intra-operative procedures[21–25]. In particular, the predicted resistivity ranges are at the lower end of the full reported range of cortical bone/skull resistivities (i.e. 0.4 – 84 kΩcm which encompasses

animal, cadaver and living human measurements)[10,21,45,46,22–26,42–44]. With known values of patient geometric descriptors, which can be obtained from patients' standard-of-care CT scans, the predictions of patient-specific cochlear bone resistivities achieve a much smaller uncertainty, with a relative standard deviation less than 5%. Thus, our methodology could provide a method to readily deduce the *in vivo* bulk resistivity of individual patient's cochlear bone matrix via CI telemetry. This could be useful in monitoring otic bone demineralization conditions such as otosclerosis in future work.

Discussion

We created a physical library of 3D printed biomimetic cochlear models, which closely captures the reported broad spectrum of EFI profiles of CI patients at off-stimulation positions that describes the electrical conduction through tissues[9]. 3D printed cochlear models were designed with resistivity-tuneable electro-mimetic bone matrices. These physical models displayed suitable mechanical stiffness for geometrically-guided CI insertion, while limiting damage to CI electrodes during insertion. It is noted that the biomimetic cochleae did not account for the frictional force generated during CI insertions under the basilar membrane in human cochleae, which may cause electrode array buckling or even intracochlear trauma affecting CI performance[47,48]. We suggest that friction could have attributed to the localised buckling configuration of the CI electrode array captured in the 3D model giving the 'mid-dip' EFI.

Our neural network model trained by measurements of 3D printed biomimetic cochleae (3PNN) constitutes a simple 5-parameter model that can readily extract data and information from CI patients under established clinical procedures. The potential broad and non-case specific applicability of 3PNN is demonstrated by the fact that the neural network was trained

by experimental EFIs measured by CI^{1J}, but off-stimulation EFIs of patients implanted with CI^{SlimJ} (up to a position of 18.5 mm along the cochlear lumen) can be successfully inferred without further model adjustment and re-calibration. Therefore, the framework has a potential capability of forecasting the post-operative electrical performances of CIs from different manufacturers, hence assisting the development of CIs tailored to patient anatomy. Comparing to conventional animal and cadaver models, the 'print-and-learn' concept proposed here offers a physical-manipulatable, ethical and economic approach, which may help reduce the need for animal experiments and, at the same time, provide a sufficient statistical predictive power for preliminary CI testing.

The 3D printed biomimetic cochleae offer a robust physical means to capture the variability in anatomical-guided CI insertion, and replicate the ionic conduction and the electron-ion interaction in cochleae with implanted CIs. The 3PNN framework could provide an important tool for solving the 'volume conduction' problem, the first step in computational neuroengineering for modelling electrical stimulation in a biological structure[19]. Further studies that evaluate the correlation between the intracochlear voltage distribution and the excitation of neural cells will be of particular benefit to expand the use of 3PNN in modelling the excitation spread at the neuronal level.

The ability of 3PNN to deduce patient-specific *in vivo* resistivity of the cochlear tissue by CI telemetry provides a valuable reference for cochlear bioelectric research. We anticipate that this unique capability might enable long-term monitoring of patients' cochlear health after CI implantation. For example, it has been suggested that the electrical properties of cochlear tissues can be affected by a variety of physiological and otologic diseases, such as post-implantation fibrosis and neo-ossification, post-operative electrode extrusion and

medications[13,49,50]. Hence, the cochlear tissue resistivities informed by patients' EFI profiles might be used as a diagnostic indicator to detect early abnormalities, without resorting to ionizing radiation of patients (which particularly should be avoided in children). With the rising usage of neuromodulating electronic implants, we anticipate that our 'print-and-learn' electroanatomical framework could facilitate the optimisation process and the pre-clinical screening of bioelectronic implant prototypes, beyond its applications in CIs.

References

1. Schiavone, G. & Lacour, S. P. Conformable bioelectronic interfaces: Mapping the road ahead. *Sci. Transl. Med.* (2019).
2. Birmingham, K. *et al.* Bioelectronic medicines: A research roadmap. *Nature Reviews Drug Discovery* vol. 13 399–400 (2014).
3. Famm, K., Litt, B., Tracey, K. J., Boyden, E. S. & Slaoui, M. A jump-start for electroceuticals. *Nature* (2013).
4. Dieter, A., Duque-Afonso, C. J., Rankovic, V., Jeschke, M. & Moser, T. Near physiological spectral selectivity of cochlear optogenetics. *Nat. Commun.* (2019).
5. Macherey, O. & Carlyon, R. P. Cochlear implants. *Current Biology* (2014).
6. Drennan, W. R., Svirsky, M. A., Fitzgerald, M. B. & Rubinstein, J. T. Mimicking Normal Auditory Functions with Cochlear Implant Sound Processing : Past, Present, and Future. in *Cochlear Implants* (eds. Waltzman, S. B. & Roland, J. T.) 47–60 (Thieme Medical Publishers, Incorporated, 2014).
7. Ben-Menachem, E. Vagus-nerve stimulation for the treatment of epilepsy. *Lancet Neurology* (2002).
8. Vöröslakos, M. *et al.* Direct effects of transcranial electric stimulation on brain circuits in rats and humans. *Nat. Commun.* (2018).
9. Vanpoucke, F. J., Zarowski, A. J. & Peeters, S. A. Identification of the impedance model of an implanted cochlear prosthesis from intracochlear potential measurements. *IEEE Trans. Biomed. Eng.* (2004).
10. Frijns, J. H. M., de Snoo, S. L. & Schoonhoven, R. Potential distributions and neural excitation patterns in a rotationally symmetric model of the electrically stimulated

cochlea. *Hear. Res.* (1995).

11. Shepherd, R. K., Hatsushika, S. & Clark, G. M. Electrical stimulation of the auditory nerve: The effect of electrode position on neural excitation. *Hear. Res.* (1993).

12. Nogueira, W., Schurzig, D., Büchner, D., Penninger, R. T. & Würfel, W. Validation of a cochlear implant patient-specific model of the voltage distribution in a clinical setting. *Front. Bioeng. Biotechnol.* (2016).

13. Maura K. Cosetti. Intraoperative Monitoring During Cochlear Implantation. in *Cochlear Implants* (eds. Susan B. Waltzman & J. Thomas Roland) 100–107 (Thieme Medical Publishers, Incorporated, 2014).

14. Wong, P. *et al.* Development and validation of a high-fidelity finite-element model of monopolar stimulation in the implanted Guinea pig cochlea. *IEEE Trans. Biomed. Eng.* (2016).

15. Adunka, O., Kiefer, J., Unkelbach, M. H., Lehnert, T. & Gstoettner, W. Development and evaluation of an improved cochlear implant electrode design for electric acoustic stimulation. *Laryngoscope* (2004).

16. Huang, C. Q., Shepherd, R. K., Carter, P. M., Seligman, P. M. & Tabor, B. Electrical stimulation of the auditory nerve: Direct current measurement in vivo. *IEEE Trans. Biomed. Eng.* (1999).

17. Ekdale, E. G. Form and function of the mammalian inner ear. *J. Anat.* (2016).

18. Opitz, A., Falchier, A., Linn, G. S., Milham, M. P. & Schroeder, C. E. Limitations of ex vivo measurements for in vivo neuroscience. *Proc. Natl. Acad. Sci. U. S. A.* (2017).

19. Romeni, S., Valle, G., Mazzoni, A. & Micera, S. Tutorial: a computational framework for the design and optimization of peripheral neural interfaces. *Nat. Protoc.* **15**, 3129–3153 (2020).

20. Malherbe, T. K., Hanekom, T. & Hanekom, J. J. The effect of the resistive properties of bone on neural excitation and electric fields in cochlear implant models. *Hear. Res.* (2015).

21. Tang, C. *et al.* Correlation between structure and resistivity variations of the live human skull. *IEEE Trans. Biomed. Eng.* (2008).

22. Akhtari, M. *et al.* Conductivities of three-layer live human skull. *Brain Topogr.* (2002).

23. Hoekema, R. *et al.* Measurement of the conductivity of skull, temporarily removed during epilepsy surgery. *Brain Topogr.* (2003).

24. Oostendorp, T. F., Delbeke, J. & Stegeman, D. F. The conductivity of the human skull:

Results of in vivo and in vitro measurements. *IEEE Trans. Biomed. Eng.* (2000).

25. Charles C. Finley, Wilson, B. S. & Mark W. White. Models of Neural Responsiveness to Electrical Stimulation. in *Cochlear Implants : Models of the Electrically Stimulated Ear* (eds. Josef M. Miller & Francis A. Spelman) 55–96 (Springer, 1990).

26. Balmer, T. W., Vesztergom, S., Broekmann, P., Stahel, A. & Büchler, P. Characterization of the electrical conductivity of bone and its correlation to osseous structure. *Sci. Rep.* (2018).

27. Kolesky, D. B. *et al.* 3D bioprinting of vascularized, heterogeneous cell-laden tissue constructs. *Adv. Mater.* (2014).

28. Advanced Bionics. *HiRes 90K® Surgeon's Manual for the HiFocus® Helix and HiFocus® 1j Electrodes*. (2005).

29. Armin Bunde & Jan W. Kantelhardt. Diffusion and Conduction in Percolation Systems – Theory and Applications. in *Diffusion in Condensed Matter* (eds. Heitjans, P. & Jörg Kärger) 895–914 (Springer, 2005).

30. Johnston, I. D., McCluskey, D. K., Tan, C. K. L. & Tracey, M. C. Mechanical characterization of bulk Sylgard 184 for microfluidics and microengineering. *J. Micromechanics Microengineering* (2014).

31. Faes, T. J. C., Van Der Meij, H. A., De Munck, J. C. & Heethaar, R. M. The electric resistivity of human tissues (100 HZ-10 MHZ): A meta- analysis of review studies. *Physiological Measurement* (1999).

32. Guimarães, C. F., Gasperini, L., Marques, A. P. & Reis, R. L. The stiffness of living tissues and its implications for tissue engineering. *Nature Reviews Materials* (2020).

33. Rho, J. Y., Tsui, T. Y. & Pharr, G. M. Elastic properties of human cortical and trabecular lamellar bone measured by nanoindentation. *Biomaterials* (1997).

34. Yang, C. & Suo, Z. Hydrogel ionotronics. *Nature Reviews Materials* (2018).

35. A J Pearmain & A G Clegg. Insulators. in *Electrical Engineer's Reference Book* (ed. G R Jones) 15 (Elsevier Ltd, 2013).

36. Davis, T. J. *et al.* Relationship between electrode-to-modiolus distance and current levels for adults with cochlear implants. *Otol. Neurotol.* (2016).

37. Erixon, E., Högstorp, H., Wadin, K. & Rask-Andersen, H. Variational anatomy of the human cochlea: Implications for cochlear implantation. *Otol. Neurotol.* (2009).

38. Pelliccia, P. *et al.* Cochlea size variability and implications in clinical practice. *Acta Otorhinolaryngol. Ital.* (2014).

39. Mori, M. C. & Chang, K. W. CT analysis demonstrates that cochlear height does not

change with age. *Am. J. Neuroradiol.* (2012).

40. Horch, K. W. & Burgess, P. R. Peripheral Nervous System. in *Neuroprosthetics: Theory and Practice* (eds. Kenneth W. Horch & Gurpreet S. Dhillon) 30–45 (World Scientific Publishing Co.Pte. Ltd., 2004).

41. Rattay, F. The basic mechanism for the electrical stimulation of the nervous system. *Neuroscience* (1999).

42. Akhtari, M. *et al.* Conductivities of three-layer human skull. *Brain Topogr.* (2000).

43. Law, S. K. Thickness and resistivity variations over the upper surface of the human skull. *Brain Topogr.* (1993).

44. Saha, S. & Williams, P. A. Electric and Dielectric Properties of Wet Human Cortical Bone as a Function of Frequency. *IEEE Trans. Biomed. Eng.* (1992).

45. Micco, A. G. & Richter, C. P. Electrical resistivity measurements in the mammalian cochlea after neural degeneration. *Laryngoscope* (2006).

46. Briaire, J. J. & Frijns, J. H. M. Field patterns in a 3D tapered spiral model of the electrically stimulated cochlea. *Hear. Res.* (2000).

47. Todd, C. A., Naghdy, F. & Svehla, M. J. Force application during cochlear implant insertion: An analysis for improvement of surgeon technique. *IEEE Trans. Biomed. Eng.* (2007).

48. Zeng, F. G., Rebscher, S., Harrison, W., Sun, X. & Feng, H. Cochlear Implants: System Design, Integration, and Evaluation. *IEEE Rev. Biomed. Eng.* (2008).

49. Frijns, J. H. M., Kalkman, R. K. & Briaire, J. J. Stimulation of the facial nerve by intracochlear electrodes in otosclerosis: A computer modeling study. *Otol. Neurotol.* (2009).

50. Carré, F., Achard, S., Rouillon, I., Parodi, M. & Loundon, N. Hearing impairment and osteogenesis imperfecta: Literature review. *European Annals of Otorhinolaryngology, Head and Neck Diseases* (2019).

51. Pietsch, M. *et al.* Spiral Form of the Human Cochlea Results from Spatial Constraints. *Sci. Rep.* (2017).

52. Jiang, C., de Rijk, S. R., Malliaras, G. G. & Bance, M. L. Electrochemical impedance spectroscopy of human cochleas for modeling cochlear implant electrical stimulus spread. *APL Mater.* **8**, 1–8 (2020).

53. Fedorov, A. *et al.* 3D Slicer as an image computing platform for the Quantitative Imaging Network. *Magn. Reson. Imaging* (2012).

54. Hornik, K., Stinchcombe, M. & White, H. Multilayer feedforward networks are

universal approximators. *Neural Networks* (1989).

55. Abadi, M. *et al.* TensorFlow: A system for large-scale machine learning. in *Proceedings of the 12th USENIX Symposium on Operating Systems Design and Implementation, OSDI 2016* (2016).

56. Kingma, D. P. & Ba, J. L. Adam: A method for stochastic optimization. in *3rd International Conference on Learning Representations, ICLR 2015 - Conference Track Proceedings* (2015).

57. Kohavi, R. A Study of Cross-Validation and Bootstrap for Accuracy Estimation and Model Selection. *Int. Jt. Conf. Artif. Intell.* (1995).

58. Toni, T., Welch, D., Strelkowa, N., Ipsen, A. & Stumpf, M. P. H. Approximate Bayesian computation scheme for parameter inference and model selection in dynamical systems. *J. R. Soc. Interface* (2009).

59. Clerx, M. *et al.* Probabilistic Inference on Noisy Time Series (PINTS). *J. Open Res. Softw.* **7**, 23 (2019).

60. Advanced Bionics. *Surgeon Manual for the HiRes™ Ultra Cochlear Implant with the HiFocus™ SlimJ and HiFocus™ Mid-Scala Electrodes*. (2016).

Acknowledgements

This work was supported by the European Research Council (ERC-StG, 758865), the Cambridge Hearing Trust and the Evelyn Trust. I.M.L. acknowledges the financial support from the W D Armstrong Trust. C.J. acknowledges the support from the Wellcome Trust. C.L.L. acknowledges the financial support from the Clarendon Scholarship Fund. S.R.D.R. acknowledges the financial support from the Baroness de Turckheim Fund, Trinity College Cambridge. We thank Advanced Bionics Corporation® for providing cochlear implants and software on this research, Anthony Dennis for technical assistance with micro-CT imaging and Tomasz Matyz for his help with the anonymised patients' CT scans.

Author contributions

I.M.L., C.J., M.B. and Y.Y.S.H. conceived the project. I.M.L. performed majority of the experiments and data analysis including 3D printing and creation of biomimetic cochlear EFI

library. C.J. performed the EIS experiments. C.L.L. developed the neural network model and assisted with part of the data analysis. I.M.L. performed the neural network model optimisation and simulations. C.J., S.R.D.R., Y.C.T. and M.B. assisted with the anonymised patient's data collection. Y.Y.S.H., G.G. and M.B. provided result interpretation. M.P.F.S. performed the mechanical deformation analysis. I.M.L. and Y.Y.S.H. wrote the initial manuscript. Y.Y.S.H and M.B. supervised the project. All authors discussed the results and revised the manuscript.

Competing interests

M.B. received research funding from Advanced Bionics®, Cochlear Corporation®, and in-kind contribution from MED-EL® on other research areas but not on the present study. The remaining authors declare no competing interests.